Evolution of cellular structures during $Ge_{1-x}Si_x$ single-crystal growth by means of a modified phase-field method

W. Miller
Leibniz Institute for Crystal Growth (IKZ), Max-Born-Str. 2, 12489 Berlin, Germany

I. Rasin
Department of Chemical Engineering, Technion, 32000 Haifa, Israel

D. Stock
Innovent Jena, Prüssingstr. 27b, 07745 Jena, Germany

(Received 24 July 2008; revised manuscript received 29 September 2009; published 17 May 2010)

We have studied the evolution of cellular structures in $Ge_{1-x}Si_x$ single-crystal growth as a function of process parameters. Because these structures are much larger than those occurring during the solidification of metals, we developed a modified phase-field method, which is able to handle these structure within reasonable computer times using the real material parameters. The model has been tested for computing equilibrium shapes of crystals, dendritic growth, and cellular growth of Ni_xCu_{1-x}. We also performed classical molecular dynamics calculations in order to compute the diffusion coefficients of Si and Ge in melts of various compositions.

DOI: 10.1103/PhysRevE.81.051604 PACS number(s): 81.10.Aj, 81.10.Fq, 02.70.Bf, 02.70.Ns

I. INTRODUCTION

The evolution of cellular structures during the solidification of metals is of great interest for the quality of the solidified material. In the case of single-crystal growth in most cases cellular growth is avoided by choosing the right growth parameters but there are several examples, where a well-defined cellular structure is the prerequisite for the final functionality of the material. One example are $Ge_{1-x}Si_x$ single crystals used to build up lenses for hard X and gamma rays (see, e.g., [1,2]).

Numerical calculations of the pattern formation of cellular or dendritic structures are still very challenging because the evolution is very sensitive to material and processes parameters. Unfortunately, material parameters are often not well known which needs additional computations on a much smaller time and length scale like, e.g., molecular dynamics or *ab initio* calculations. For instance, the diffusion coefficient for Si in the Ge-rich melt is one of these parameters. We have performed molecular dynamics studies in order to compute the diffusion coefficients for both Si and Ge for different compositions of the melt.

Another problem of computing the pattern formation is the complicated topology of the phase boundary, which might occur during its evolution. During the last years phase field methods has emerged as powerful tools to handle such situations. They use a continuous order parameter to distinguish between solid and liquid. Therefore, the interface is not sharp but diffuse, which dispenses us from a using a moving grid. First introduced for pure substances [3,4] the methods have been extended to binary alloys [5–7], eutectics, peritectics [8,9], and others.

In general, they have been used for large constitutional undercooling, where the resulting structures are of the order some μm. In the case of Czochralski growth of $Ge_{1-x}Si_x$ the structures are of about ten times larger and a high number of grid point in the vicinity of the phase boundary is needed in order to resolve the Gibbs-Thomson effects by the phase-field method and to cover a crystal area of sufficient size for analyzing the growth patterns. We developed a modified phase field model which allows to use a reasonable thickness of the interface while taking the physical Gibbs-Thomson coefficient of the system.

The first phase-field model for binary alloys was introduced by Wheeler, Boettinger, and McFadden (WBM model) [7] assuming that the concentrations of the solid and liquid phase in the diffuse interface are identical. Their model has a constraint on the interface thickness because the chemical energy in the diffuse interface puts an extra contribution to the surface energy. This can be avoided by introducing an "antitrapping" term [5,10] or by introducing separate concentration fields for the liquid and solid phase [6]. We used the latter (KKS model, named after the authors Kim, Kim, Suzuki) for our computations and recall it shortly in Sec. II C.

II. PHASE-FIELD METHOD

A. Phase-field model for pure substances

Solidification and melting of pure substances can be described by the thermal field T and an order parameter field ϕ. The phase-field variable ϕ switches continuously between pure liquid state ($\phi=0$) and pure solid state ($\phi=1$). The equations for the time evolution of T and ϕ can be derived in a thermodynamically consistent way from the definition of the internal energy and the entropy of the system [3,11]:

$$\tau\partial_t\phi = \xi_S^2\Delta\phi - W\partial_\phi g - \frac{L}{T_m^2}\partial_\phi p\tilde{T}, \tag{1}$$

$$\partial_t T = D_T \Delta T + \frac{L}{c_p}\partial_t h(\phi), \tag{2}$$

where D_T, L, and c_p are the thermal diffusivity, the latent heat, and the specific heat, respectively. $\tilde{T}$ is the temperature related to the melting point temperature T_m: $\tilde{T}=T-T_m$. $\xi_S/\sqrt{2W}$ is the length scale of the model and defines the surface tension and τ/W is the time scale and defines the relaxation of the system. The function $g(\phi)$ represents the potential of the system in the equilibrium state and is mostly taken as a double-well potential:

$$g(\phi) = \phi^2(1-\phi)^2, \tag{3}$$

and W is the height of the barrier between the wells. The relations between the model and the physical parameters (kinetic coefficient μ and capillary length d_0) can be obtained by an asymptotic analysis for a thin interface [12]:

$$\mu^{-1} = a_1 \frac{\tau T_m^2 \sqrt{W}}{L\xi_S} - a_2 \frac{\xi_S L}{c_p D_T \sqrt{W}}, \tag{4}$$

$$d_0 = a_1 \frac{\xi_S c_p T_m^2 \sqrt{W}}{L^2}, \tag{5}$$

where a_1 and a_2 are constants which depend on the choice of $p(\phi)$ and $h(\phi)$. $p(\phi)$ is a monotonically increasing function which fulfills the conditions $p(0)=0$, $p(1)=1$, $\partial_\phi p(0)=\partial_\phi p(1)=0$. Different polynoms have been tested (see [12,13]) and a polynom of fifth order seems to be a good choice for stability and computational reasons:

$$p(\phi) = 30\left(\frac{\phi^3}{3} - \frac{\phi^4}{2} + \frac{\phi^5}{5}\right). \tag{6}$$

By strict thermodynamical derivation $h(\phi)$ should be same function as $p(\phi)$. For practical reasons often $h(\phi)=\phi$ is chosen regardless of the function $p(\phi)$. Calculations with different functions for $h(\phi)$ exhibited same results as were shown by Karma and Rappel [12] as well as by Kim *et al.* [13].

Using $p(\phi)$ as defined by Eq. (6) and $h(\phi)=\phi$ the constants a_1 and a_2 are given by

$$a_1 = \frac{1}{3\sqrt{2}}, \quad a_2 = 0.3519. \tag{7}$$

For the case of equilibrium Eq. (1) can be solved in one dimension yielding an expression for the phase field as a function of the distance x to the interface:

$$\phi = \frac{1}{2}\left(1 + \tanh\frac{\sqrt{W}x}{\sqrt{2}\xi_S}\right). \tag{8}$$

B. Modified phase-field model

Since there is only one length scale in the phase-field model as introduced in the previous section, namely, $\xi_S/\sqrt{2W}$, the width of the diffuse interface $w_\phi = 6\xi_S/\sqrt{2W}$ is coupled with the capillary length d_0. In order to ensure a numerically stable system the barrier between liquid and solid state in the temperature-driven system should be not too small compared to the isothermal case. For $L\tilde{T}/WT_m^2=1$ the barrier in one direction is only 0.2% of the isothermal value. Using this value as a limiting criteria and take Eq. (5) into account we can derive the relation

$$\frac{1}{18}\frac{c_p}{L}\tilde{T}\frac{w_\phi}{d_0} < 1. \tag{9}$$

Typically, $c_p/L \approx 10^{-3}$ K^{-1}, $d_0 \approx 10^{-10}$ m, and $\tilde{T} \approx 1-5$ K so that w_ϕ should be less than 1 μm.

Replacing $\xi^2\Delta\phi$ by a tensorial expression $\Xi_{\alpha\beta}\nabla_\alpha\nabla_\beta\phi$ allows the introduction of a second length scale in the system. In order to derive an expression for $\Xi_{\alpha\beta}$ we start from the classical phase-field equation

$$\tau\partial_t\phi = \xi_S^2[n_\alpha n_\beta \nabla_\alpha\nabla_\beta\phi + (\Delta - n_\alpha n_\beta \nabla_\alpha\nabla_\beta)\phi] - Wg_\phi + \frac{L}{T_m^2}p_\phi\tilde{T}. \tag{10}$$

The term $n_\alpha n_\beta \nabla_\alpha\nabla_\beta\phi$ corresponds to the second derivative of the phase field along an isosurface. The term $(\Delta - n_\alpha n_\beta \nabla_\alpha\nabla_\beta)\phi$ corresponds to the curvature of an isosurface. We introduce two parameters $\xi_\perp$ and $\xi_\parallel$ for the first and second terms:

$$\tau\partial_t\phi = \xi_\perp^2 n_\alpha n_\beta \nabla_\alpha\nabla_\beta\phi + \xi_\parallel^2(\Delta - n_\alpha n_\beta \nabla_\alpha\nabla_\beta)\phi - Wg_\phi + \frac{L}{T_m^2}p_\phi\tilde{T}. \tag{11}$$

The equilibrium solution in one-dimensional (1D) is the same as before and so the relation for the phase field perpendicular to the interface is given by Eq. (8) with $\xi_S \equiv \xi_\perp$. Using the same kind of asymptotic analysis for a thin interface limit as in [12] one obtains

$$\mu^{-1} = a_1 \frac{\tau T_m^2 \sqrt{W}}{L\xi_\perp} - a_2 \frac{\xi_\perp L}{c_p D_T \sqrt{W}}, \tag{12}$$

$$d_0 = a_1 \frac{\xi_\perp c_p T_m^2 \sqrt{W}}{L^2}\gamma_\xi^2. \tag{13}$$

For convenience we introduced the factor $\gamma_\xi = \xi_\parallel/\xi_\perp$. Setting

$$\Xi_{\alpha\beta} = (\xi_\perp^2 - \xi_\parallel^2)n_\alpha n_\beta + \xi_\parallel^2\delta_{\alpha\beta} \tag{14}$$

we can write Eq. (11) as

$$\tau\partial_t\phi = \Xi_{\alpha\beta}\nabla_\alpha\nabla_\beta\phi - Wg_\phi + \frac{L}{T_m^2}p_\phi\tilde{T}. \tag{15}$$

Let us analyze the advantage of the modified phase-field model vs the classical one. Condition (9) states that w_ϕ should be scaled linearly with $d_0/\tilde{T}$. The capillary length is given by Eq. (13) with $\xi_\perp = w_\phi 2\sqrt{W}/6$. Therefore, the interface thickness w_ϕ and space step Δx can be increased be taking large values of γ_ξ:

$$\frac{\Delta x^{\mathrm{mod}}}{\Delta x^{\mathrm{classical}}} = \frac{w_\phi^{\mathrm{mod}}}{w_\phi^{\mathrm{classical}}} = \gamma_\xi^{-2}. \tag{16}$$

The corresponding simulation time for an explicit finite difference scheme is scaled as

$$\gamma_\xi^{-2(N_d+2)},$$

where N_d is the number of dimensions.

The choice of γ_ξ is limited by the physics of the system considered. The interface thickness should be significantly smaller then the minimum radius of surface curvature: $w_\phi \ll r_{\mathrm{curv}}$. In addition, the temperature should not change significantly across the diffuse interface. Thus, the modified phase field model is well applicable for systems with small temperature gradients, e.g., for the solidification of Si for photovoltaic applications.

Real materials exhibit an anisotropy in the surface tension γ. Therefore, γ and d_0 are functions of the surface normal $\vec{n}$. Let $d_0(\vec{n}) = \tilde{d}_0(1+f_{d_0}(\vec{n}))$. In the phase field model the anisotropy is expressed by $\xi_S(\vec{n})$. This means that the thickness of the interface varies with the orientation. Since the anisotropy is in the order of some percent, this is only a weak effect. In the modified phase field model the anisotropy enters only $\xi_\parallel$.

We write $\xi_\parallel(\vec{n}) = \tilde{\xi}_\parallel(1+f_\xi(\vec{n}))$ and define γ_ξ as $\gamma_\xi = \tilde{\xi}_\parallel/\xi_\perp$ so that γ_ξ is independent of the growth direction $\vec{n}$. The continuum limit should now converge towards Herring's instead of the Gibbs-Thomson equation leading to $d_0 + \partial_{\vec{n}}^2 d_0$ on the left-hand side of Eq. (13). On the right hand side we have to replace γ_ξ^2 by $\gamma_\xi^2(1+f_\xi(\vec{n}))$. Thus, we obtain the relation

$$1 + f_\xi(\vec{n}) = \sqrt{1 + f_{d_0}(\vec{n}) + \partial_{\vec{n}}^2 f_{d_0}(\vec{n})}. \tag{17}$$

Note that Eq. (17) is undefined for the missing directions in a crystal $(1+f_{d_0}(\vec{n}) + \partial_{\vec{n}}^2 f_{d_0}(\vec{n}) < 0)$. Therefore, a cutoff is introduced in the numerical calculations guaranteeing that $1 + f_{d_0}(\vec{n}) - \partial_{\vec{n}}^2 f_{d_0}(\vec{n}) > 0$. In all calculations of this paper we set the cutoff as 1×10^{-6}. $\xi_\perp$ is unaffected and so is the width of the diffuse interface and also the relaxation time τ [see Eq. (12)]. Consequently, the phase field equations are not the same for the classical and the modified model even if $\gamma_\xi = 1$. McFadden *et al.* showed that the classical phase field model gives in a first-order approach of the sharp interface limit Herring's equation [14].

The derivation given above is both for two-dimensional (2D) and three-dimensional (3D). In the rest of this paper we will give several examples for the application of the modified phase field model in 2D. Applying the model to 3D is straightforward but computations are much more time consuming. Firstly, we performed calculations for three types of problems in order to test the accuracy of the modified phase field model. All computations have been performed with $\gamma_\xi = 1$. Firstly, we investigated the evolution of a small nucleus with isotropic surface tension. The change in its radius is described by

$$\partial_t r = \mu\left(\tilde{T} + \frac{\Gamma}{r}\right), \tag{18}$$

with the analytic solution

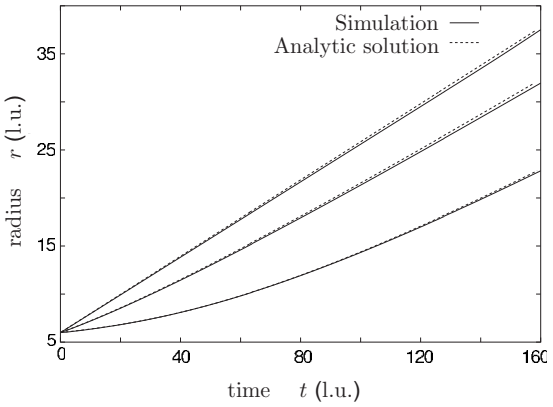

FIG. 1. Evolution of the crystal radius (in lattice units, l.u.) for three different capillary lengths and comparison with the analytic solution [Eq. (19)]. $r_0 = 6$ l.u., $\tilde{T} = -0.55$, $\mu = 0.361$ l.u., $dt = 0.016$ l.u., and $\Gamma = 2.77\gamma$ l.u. with $\gamma = 1.0, \sqrt{1/2}, 0.1$ for bottom, middle, top line, respectively.

$$t = \frac{\Gamma}{\tilde{T}^2\mu}\log\left(\frac{r\tilde{T}+\Gamma}{r_0\tilde{T}+\Gamma}\right) - \frac{r-r_0}{\tilde{T}\mu}, \tag{19}$$

where r_0 is the radius at $t=0$. The numerical results for three different Gibbs-Thomson coefficients are presented together with the analytic solution in Fig. 1.

The next example is the curvature driven flow in an isothermal environment. Starting from a circle the shape of the crystal will change to its equilibrium shape, which is given by the Wulff construction. The equilibrium shape is given in parametric form by $\vec{r}(\vec{n}) = 2T_m/[(T_m - T)L_V]\vec{\chi}$, where L_V means the latent heat per volume [15]. In two dimensions $\vec{\chi}$ is obtained via

$$\chi_x = \gamma\cos\theta - (d\gamma/d\theta)\sin(\theta), \tag{20}$$

$$\chi_y = \gamma\sin\theta + (d\gamma/d\theta)\cos(\theta). \tag{21}$$

We use a fourfold symmetry for the surface tension:

$$\gamma(\vec{n}) = \gamma_0(1 + \epsilon_4\cos 4\theta), \tag{22}$$

where ϵ_4 is the anisotropy parameter. The computed and analytic shapes are shown in Fig. 2.

The third example is the 2D dendritic growth of a pure material into an undercooled melt. For such a system in a steady-state mode the theory is well developed and an equation for the tip velocity can be derived (see, e.g., [12]). In Fig. 3 the measured dimensionless tip velocity is plotted for two calculations of different strength of anisotropy. The dimensionless tip velocity is given by rescaling the tip velocity v_{tip} with the capillary length d_0 (characteristic length scale) and the thermal diffusivity D (defines the characteristic time scale): $\tilde{v}_{\mathrm{tip}} = v_{\mathrm{tip}} d_0/2D$.

C. Phase-field model for binary alloys

In addition to pure substances we have a third scalar field, namely, concentration of the solute $c(\vec{r},t)$, which also governs the phase transition. In this paper we will treat the tem-

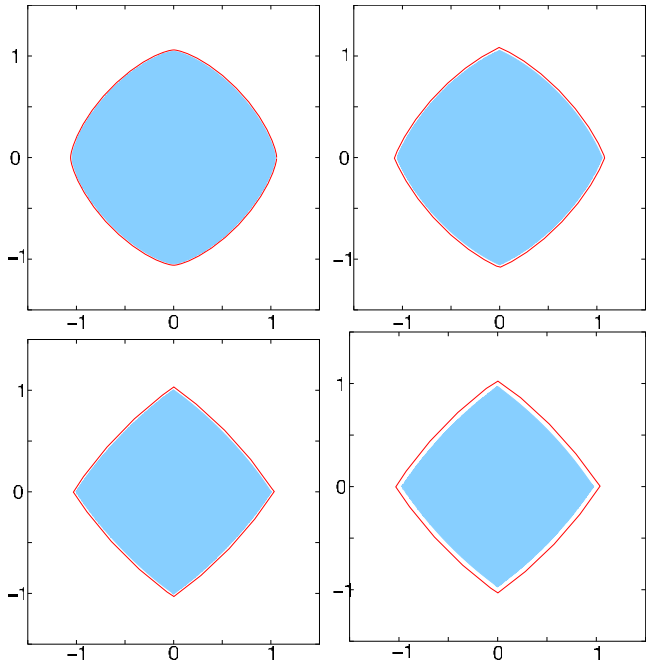

FIG. 2. (Color online) Equilibrium shapes for crystals of different values for anisotropy of surface tension (from top left to bottom right): ϵ_4=0.05,0.1,0.2,0.5. Filled area and line represent the result of the phase-field calculation and the analytic solution, respectively.

perature as a static quantity affecting the evolution of the scalar fields only via external conditions. Instead of equations Eqs. (1) and (2) we now have the following set of coupled nonlinear advection-reaction-diffusion equations:

$$\tau\partial_t\phi = \xi_S^2\Delta\phi - W\partial_\phi g(\phi) + \frac{L}{T_m^2}\Theta\partial_\phi p(\phi), \tag{23}$$

$$\partial_t c = \nabla[D(\phi)\,\nabla\, c + D(\phi)(c_l - c_s)\,\nabla\, p(\phi)] + \vec{v}\,\nabla\, c_l, \tag{24}$$

where c is the concentration and D is the diffusion coefficient of the solvent. c_l and c_s are the concentrations in the liquid and solid phases, respectively. For ϕ=0 and ϕ they

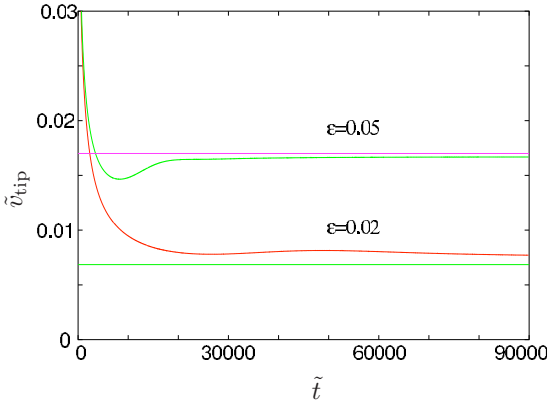

FIG. 3. (Color online) Normalized velocity of the tip for dendritic growth into an undercooled melt (St=0.55). The straight lines indicate the analytic solutions.

correspond to the liquidus and solidus curves, respectively. v is the (local) velocity of the flow field.

From the supposed equality of chemical potentials in the phase-field model of Kim *et al.* [6] the following relation for the concentrations can be obtained:

$$c_l = \frac{-\alpha + c + (1-p) + \sqrt{\mathcal{D}}}{2(1-p)}, \tag{25}$$

$$c_s = \frac{\alpha + c + p - 1 - \sqrt{\mathcal{D}}}{2p}, \tag{26}$$

$$\mathcal{D} \equiv (\alpha + c + p - 1)^2 - 4cp\alpha, \tag{27}$$

where α is a constant, which depends on temperature and material parameters. It is related to the phase diagram of the system. The constitutional undercooling Θ is given by

$$\Theta = \frac{T^2}{cL_A + (1-c)L_B}\left(L_B(T^{-1} - T_{m,B}^{-1}) + \frac{R}{V_m}\ln\frac{1-c_l}{1-c_s}\right), \tag{28}$$

where L_A, L_B are the latent heats per unit volume of components A and B, c is the concentration of component A and $T_{m,B}$ the melting point temperature of component B. R and V_m are the gas constant and the molar volume, respectively.

Finally, we have to ensure zero diffusivity in the solid phase. The simplest approach is

$$D(\phi) = D_0(1-\phi). \tag{29}$$

We also use the switch function $p(\phi)$ for this purpose:

$$D(\phi) = D_0(1 - p(\phi)). \tag{30}$$

III. CONFIGURATION AND NUMERICAL PROCEDURE

We have taken a small region including the interface from the entire system of Czochralski growth. The diameter of the crystal is typically 3 cm, whereas we have domains in the order of millimeters. Our domain was rectangular with periodic boundary conditions perpendicular to the growth direction. Per definition, the growth direction is up-down, i.e., in the $-y$ direction. The crystal was placed in the top part of the domain. The temperature profile was defined by a constant temperature gradient, G_T, and was moving in time t with a constant velocity $v_{\rm pull}$, representing the pulling velocity of the Czochralski process. Thus the local temperature can be defined by the expression

$$T(x,y) = T_0 + G_T(y + v_{\rm pull}t), \quad G_T < 0.$$

The simulation domain follows the front of crystallization. In order to keep the interface within this domain we apply the following strategy: the computational domain "moves"' with the advancing solidification front. This is obtained by chopping the solid volume top and adding a corresponding liquid volume at the bottom of the computational volume. The phase-field Eq. (23) is solved by a special nine-point-stencil

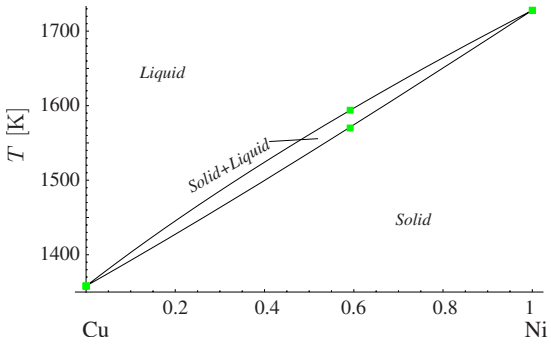

FIG. 4. (Color online) Phase diagram for Ni_xCu_{1-x}. Data points from [22], line constructed from phase field model.

finite difference scheme [16] similar to that of Karma *et al.* [17]. The phase-field is computed only in the region where $10^{-4} < \phi < 1-10^{-4}$. In order to initialize the instabilities we put a dynamical random noise of maximum 1% in the constitutional undercooling. Since we use an explicit finite difference scheme there is an upper limit for the time step Δt. The diffusion constant for the moving phase field is given by $D_\phi = \xi_\perp^2/\tau$. Taking the sharp interface limit [second term in Eq. (12) is neglected] the diffusion constant can be expressed by

$$D_\phi = \Gamma\mu/\gamma_\xi^2. \tag{31}$$

The linear stability analysis restricts

$$D_\phi^* = D_\phi \Delta t/\Delta x^2 \tag{32}$$

to values $D_\phi^* < 0.25$ in two dimensions. This gives an upper limit for the time step in relation to the grid spacing Δx:

$$\Delta t < 0.25 \Delta x^2 \gamma_\xi^2 \Gamma^{-1} \mu^{-1}. \tag{33}$$

The evolution equation for the concentration is solved by a multirelaxation lattice Boltzmann scheme [18]. Though it is explicit in time it does not suffer from stability constraints as mentioned above. Therefore, the setting of the time step in our calculations is only driven by the restrictions due to solving the phase-field equation. Typically, a fixed concentration c_{l0} is used at the boundary of the melt (Dirichlet boundary condition), which is the bottom boundary in our definitions:

$$c(l_y,t) = c_{l0}. \tag{34}$$

In order to achieve the concentration of Si in the solid, which was observed in experiments, and to avoid a large fluid domain we fix the flux (Neumann boundary condition) at the bottom by

$$J(l_y,t) = (c_{l_y,t} - c_{s0}) v_{\text{pull}}. \tag{35}$$

c_{s0} is the required mean concentration in the solid. For all computations we used a fixed uniform grid and a constant time step. In principle, the numerical schemes can be run both with an adaptive grid and an adaptive time step [19].

IV. CELLULAR GROWTH OF Ni_xCu_{1-x}

Because Ni_xCu_{1-x} is a nearly ideal solution it has been widely studied by means of phase field methods since the beginning of establishing a phase field model for binary alloys [7]. The equilibrium phase diagram (see Fig. 4) was recovered from the phase field model with the physical parameters of Ni and Cu by using the common tangent construction [7]. Later Boettinger and Warren performed a systematic numerical study of the cellular growth using the WBM model [20]. The calculations were repeated by Lan and Chang using an efficient adaptive numerical scheme [21], using the same width of the interface ($w_\phi = 4.5 \times 10^{-8}$ m). We have performed the computations with the same parameters as the previous authors (physical parameters see Table I) but using the KKS model with the modification described in Sec. II B. Two different resolutions have been used the coarser with a width of the diffuse interface of $w_\phi = 6$ l.u. and the higher one with $w_\phi = 10$ l.u.. The results are in reasonable agreement with the previous ones (see Fig. 5).

TABLE I. Physical parameters of Ni and Cu as used in [20].

	Nickel	Copper
Melting-point temperature (K)	1728	1358
Latent heat (J/m^3)	2.350×10^9	1.728×10^9
Diffusion coefficient in melt (m^2/s)	$1. \times 10^{-9}$	$1. \times 10^{-9}$

Some remarks on the WBM and the KKS model are of order. In the WBM model it is assumed that in the diffuse interface the liquid and solid phases have the same composition ($c_l \equiv c_s$). This leads to extra chemical energy depending on the thickness of the interface which contributes to the surface energy. The Gibbs-Thomson coefficient was effectively six times smaller in our calculations than in the WBM computations. All computations mentioned so far have been performed with $\gamma_\xi = 1.0$. We also performed some with $\gamma_\xi = 3.0$. We reduced the resolution by this factor, i.e., we now have a computational domain of 365×292 grid points in-

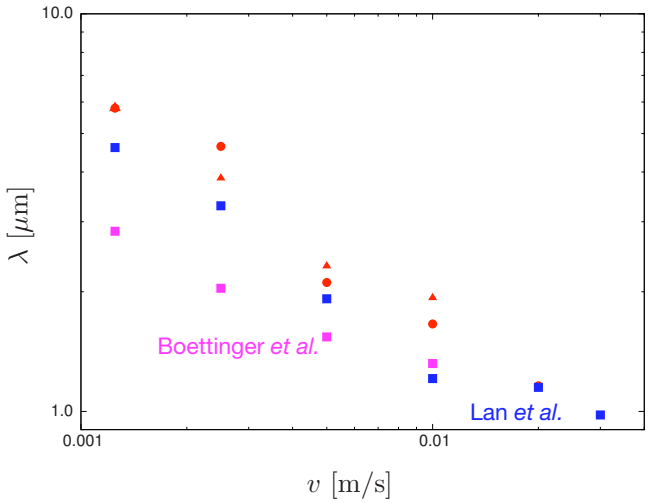

FIG. 5. (Color online) Wave length versus pulling velocity for the cellular growth of Ni_xCu_{1-x}. For comparison the results by Boettinger and Warren [20] and by Lan and Chang [21] are shown. Filled triangles represent calculations with $w_\phi = 6$ l.u. and filled circles those with $w_\phi = 10$ l.u..

TABLE II. Wave lengths for two different set of runs.

v_{pull} (ms^{-1})	λ (μm)	
	$\gamma_\xi=1$	$\gamma_\xi=3$
1.25×10^{-3}	5.8	5.6
2.5×10^{-3}	4.6	2.9
5.0×10^{-3}	2.1	2.9
1.0×10^{-2}	1.7	1.8

stead of 1094×875 ones and a diffuse interface width of $w_\phi=1.35\times10^{-7}$ m instead of $w_\phi=4.5\times10^{-8}$ m. The resolution of the diffuse interface remained 10 l.u.. Such a coarse system with $\gamma_\xi=1.0$ is unstable and will lead to a broadening of the diffuse interface and liquid trapping. The results of the runs with $\gamma_\xi=3.0$ are presented in Table II.

V. $Ge_{1-x}Si_x$

Ge and Si are completely miscible and the phase diagram for this system is shown in Fig. 6. Typically, crystals are grown either on the Si-rich or on the Ge-rich side. We consider the second case because crystals with this composition are of interest for applications in X- and gamma-ray lenses. In the region of interest liquidus and solidus can be approximated by linear relations

$$T_l = T_m^{\text{Ge}} + 1500\ \text{K}c_{\text{Si}}, \quad T_s = T_m^{\text{Ge}} + 270\ \text{K}c_{\text{Si}}, \qquad (36)$$

where T_m^{Ge} is the melting point temperature of Ge(T_m^{Ge} =1210.35 K). We will make use of this relation later in Sec.

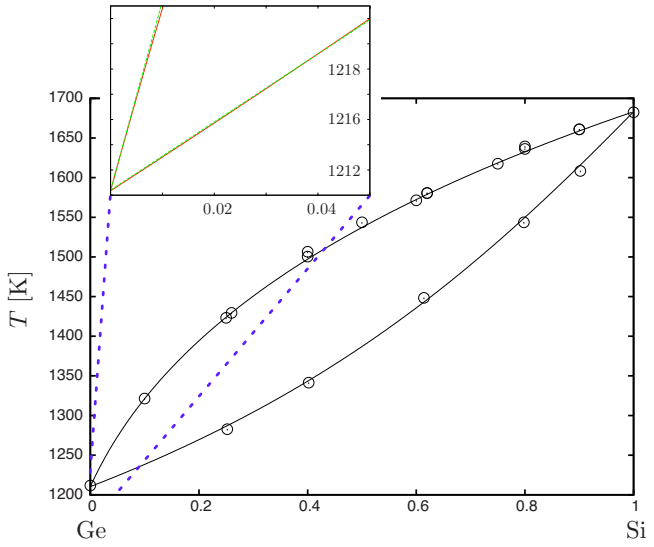

FIG. 6. (Color online) Phase diagram of the $Ge_{1-x}Si_x$ binary alloy. The region of interest for the application is magnified and shown in the upper part. The experimental values of solidus and liquidus curve are marked by circles [23]. The black lines have been computed using the free energy with temperature-dependent latent heats. In the region of interest the solidus and liquidus lines can be approximated by 1210.4 K+270 K c_{Si} and 1210.4 K+1500 K c_{Si}, respectively. The solid (red) line was computed by the free energy and the (green) dashed line by the linear approximation [Eq. (36)]. The lines are nearly undistinguishable.

V B. Please note that for the liquidus line only concentrations less than 0.02 are relevant.

The experimentally measured phase diagram can be recovered from the free energy using the common tangent method [7]. However, in contrary to Ni_xCu_{1-x} we have to introduce a temperature-dependent latent heat $L^X=L_0^X(1+\alpha_X T)$, where L_0^X are the latent heats of the pure materials X=Si,Ge at their melting-point temperatures. We adjusted the parameters α_X as $\alpha_{\text{Si}}=2\times10^{-4}$ K^{-1} and $\alpha_{\text{Ge}}=9\times10^{-5}$ K^{-1} and observed the curves in Fig. 6.

A. Diffusion coefficients for Si and Ge

One critical material parameter in constitutional undercooling is the diffusion coefficient. In the literature different values for the diffusion coefficients of Ge and Si in the liquid phase can be found. Experimental measurements were made more than 30 years ago by Romanenko und Smirnow [24]. They performed solute segregation studies in Czochralski grown crystals in the range of nearly pure Ge($D_{\text{Si}}\approx2\times10^{-8}$ m^2/s) to nearly pure Si($D_{\text{Si}}\approx1\times10^{-7}$ m^2/s). Dismukes and Yim used $D_{\text{Si}}\approx3\times10^{-8}$ m^2/s in their paper on interface stability criteria [25]. They gave a citation for this value but the cited paper [J. Appl. Phys. 2, 212 (1963)] does not contain a value on the diffusivity of Si. Much later, the self-diffusivity of Si was measured using pulsed laser melting technique by Sanders and Aziz [26]. They found the self-diffusion coefficient of Si at the melting point to be $D_{\text{Si}}=(4\pm0.5)\times10^{-8}$ m^2/s.

Numerical calculations by means of molecular dynamics (MD) have been performed by several authors. From ab initio MD calculations Ko *et al.* obtained diffusion values of $D_{\text{Si}}=1.9\times10^{-8}$ m^2/s and $D_{\text{Ge}}=1.5\times10^{-8}$ m^2/s for $Ge_{0.5}Si_{0.5}$ [27]. The temperature was T=1473 K, which is melting point temperature for this composition according to [28]. First-principles MD calculation are limited to very short time scales. In the cited paper it was 3.2 ps. A self diffusion coefficient of Germanium in the same range was found earlier by Kulkarni *et al.* [29] ($D_{\text{Ge}}=1.7\times10^{-8}$ m^2/s at 1400 K). More recent computations with long-time runs (66 ps) gave a value of $D_{\text{Ge}}=9.0\times10^{-9}$ m^2/s at 1253 K [30]. Other authors obtained similar results for Ge [31,32].

Classical MD calculations based on interatomic potentials can be performed over much longer periods of simulation time. For silicon, a well-established model potential consisting of sums of two-body and three-body interactions was proposed by Stillinger and Weber in 1985 [33]. They gave only a parametrization for silicon, but later a parametrization of the Stillinger-Weber model for Ge was applied by Yu *et al.* to study thin film growth [34,35] and solidification of SiGe alloys [36]. In the latter Yu *et al.* calculated diffusion coefficients of Si and Ge for a number of alloy compositions at their congruent melting point temperature. They found that the diffusion coefficients of Si and Ge do not differ very much from each other at a given composition. For $c_{\text{Si}}=0.25$ they obtained $D_{\text{Si}}=3\times10^{-9}$ m^2/s. We have performed extensive MD simulations using the Stillinger-Weber model with a parameter set given by Yu *et al.* [37] to calculate the diffusion coefficient of Si in liquid GeSi alloys for a number

TABLE III. List of computations for $v_{\mathrm{pull}}=6$ mm/h. The resolution Δx was chosen to keep the relation of the width of the diffuse interface w_ϕ and the cell depth d_{depth} of about the same order. The relaxation parameter τ is given by $\tau=3.87\times10^9\Delta x$ s J/m^4 K.

D_{Si} (m^2/s)	G_T (K/m)	$n_x\times n_y$	Δx (μm)	Δt (ms)	t_{total} (s)	d_{depth} (mm)	λ (mm)	$w_\phi/d_{\mathrm{depth}}$
3×10^{-8}	700	3000×750	20.0	300.0	1.50×10^5	10.0	12.0	2.0×10^{-2}
	900	3000×850	9.8	76.0	6.08×10^4	5.5	5.9	1.8×10^{-2}
2×10^{-8}	900	1000×700	20.00	320.0	1.60×10^5	8.7	10.0	2.3×10^{-2}
	1000	3000×750	15.00	180.0	1.44×10^5	7.9	9.0	1.9×10^{-2}
	1100	3000×800	11.90	113.0	9.04×10^3	6.4	7.1	1.9×10^{-2}
	1200	3000×850	9.33	69.6	5.57×10^4	5.2	7.0	1.8×10^{-2}
	1300	3000×850	7.15	40.9	3.27×10^4	4.2	5.4	1.7×10^{-2}
	1500	3000×950	3.67	10.7	8.56×10^3	2.7	2.2	1.4×10^{-2}
1×10^{-8}	1300	1600×800	20.00	320.0	1.60×10^5	8.0	8.0	2.5×10^{-2}
	1500	1600×800	15.00	180.0	1.17×10^5	6.7	8.0	2.2×10^{-2}
	1700	1600×800	12.00	115.0	1.15×10^5	5.4	6.4	2.2×10^{-2}
	1900	1600×1000	8.50	57.5	1.15×10^5	4.4	4.5	1.9×10^{-2}
	2500	1600×1000	5.00	20.0	4.00×10^4	2.6	4.0	1.9×10^{-2}
6×10^{-9}	1300	2000×2150	10.00	50.0	1.00×10^5	10.4	6.7	9.6×10^{-3}
	1500	2000×700	20.00	300.0	1.50×10^5	7.6	6.7	3.2×10^{-2}
	2000	3000×750	11.00	96.7	7.74×10^4	5.5	5.0	2.0×10^{-2}
	2500	3000×750	7.60	46.2	3.70×10^4	5.0	5.0	1.9×10^{-2}
	3000	3000×850	5.33	22.7	1.82×10^4	2.9	2.7	1.8×10^{-2}
1.9×10^{-9}	3000	800×1300	5.00	5.0	8.00×10^3	4.6	2.0	1.1×10^{-2}
	5000	1200×1000	5.00	20.0	5.12×10^4	2.4	2.0	2.1×10^{-2}
	8000	2000×600	2.50	5.0	2.40×10^4	1.2	1.0	2.2×10^{-2}
	10000	600×200	8.00	50.0	2.00×10^4	0.4	1.0	2.0×10^{-1}
	12000	600×200	8.00	50.0	2.50×10^4	0.1	1.0	6.2×10^{-1}
1×10^{-9}	3000	800×1300	5.00	5.0	4.00×10^3	4.5	1.3	1.1×10^{-2}
	5000	800×600	10.00	80.0	4.00×10^4	2.3	1.6	4.4×10^{-2}
	8000	1000×400	5.00	5.0	1.00×10^4	1.4	1.0	3.6×10^{-2}

of compositions c_{Si} between 0.02 and 0.25. For a given composition the simulations were done at the corresponding congruent melting temperature of the alloy as taken from [28]. The calculated Si diffusion coefficient increases linearly with c_{Si} from 4.4×10^{-9} m^2/s to 5×10^{-9} m^2/s. The applied melting temperatures of the GeSi alloys [28] based on a regular solution model are smaller than those obtained from the phase diagram in Fig. 6. For better comparison with experimental data an extension of the MD simulations to determine the appropriate alloy melting temperature is required. The obtained diffusion coefficients for Si and Ge in the liquid phase from classical MD simulations using the Stillinger-Weber interatomic potential are in general smaller than those from ab initio calculations. This difference is probably attributed to the inherent functional form of the Stillinger-Weber potential [37].

B. Cellular growth of $Ge_{1-x}Si_x$

We have performed a series of computations for different Peclet numbers $\mathrm{Pe}=l_0v_{\mathrm{pull}}/D_{\mathrm{Si}}$. l_0 is a characteristic length and can be chosen as the capillary length d_0. Because in experiments the pulling velocity was fixed to $v_{\mathrm{pull}}=6$ mm/h but the diffusion coefficient D_{Si} is not well known as discussed in the previous subsection we discuss the results in terms of physical values. We varied the temperature gradient G_T and analyzed the cell depth and wave length of the cellular structures. The average concentration in the crystal is adjusted to $\bar{c}_s=0.02$ by using the boundary condition Eq. (35). This average value is typical for most of the experiments. All parameters for the different runs are listed in Table III and the physical values are given in Table IV.

1. Cell depth

According to perturbation analysis, cellular structures can occur for temperature gradients less a critical one: $G_T<\Delta T_0v_{\mathrm{pull}}/D_{\mathrm{Si}}$ (see p. 53 in [38]). ΔT_0 is the temperature difference between liquidus and solidus at the concentration of the solid. Using the relations of Eq. (36) we obtain $\Delta T_0=24.6$ K for $c_s=0.02$. Cell depth and wave length should go towards zero when approaching the critical value. The critical inverse temperature gradient for the pulling velocity of $v_{\mathrm{pull}}=6$ mm/h is given by

TABLE IV. Parameters for the simulations of the growth of $Ge_{1-x}Si_x$ crystal.

Parameter	Value
Latent heat Si	4.225×10^9 J/m^3
Latent heat Ge	2.82×10^9 J/m^3
Gibbs-Thomson coeff.	6.0×10^{-9} K m
Si concentration in crystal	≈0.02
Width of transition region	10 l.u.

$$(1/G_T)_{\rm cr} = 2.5\times10^4 \ {\rm sm}^{-1}\,{\rm K}^{-1}\,D_{\rm Si}. \quad (37)$$

In the following we will analyze the cell depth and the wave length of the cellular pattern. We start with the cell depth, which is plotted vs the inverse temperature gradient for the different diffusion coefficients (Fig. 7). For $d_{\rm depth}=0$ we use the critical value obtained by Eq. (37). A linear dependence is observed for all diffusion coefficients:

$$d_{\rm depth} = d_d(D_{\rm Si}) + \frac{\Delta_d T}{G_T}. \quad (38)$$

The coefficient $\Delta_d T$ is the same for all diffusion coefficients. It was determined by shifting every curve in Fig. 7 by $-(1/G_T)_{\rm cr}$ and yields $\Delta_d T = 14.7 \pm 1.6$ K. d_d can be simply computed from the fact that all curves cross $(1/G_T)_{\rm cr}$ at $d_{\rm depth}\equiv 0$:

$$d_d(D_{\rm Si}) = -\frac{D_{\rm Si}\Delta_d T}{v_{\rm pull}\Delta T_0}. \quad (39)$$

Because of the constant temperature gradient the temperature difference between top and bottom of a cell can be computed via $\Delta T = G_T d_{\rm depth}$. If we are in a steady-state situation, i.e., the shapes of the cells are not changing in time, the

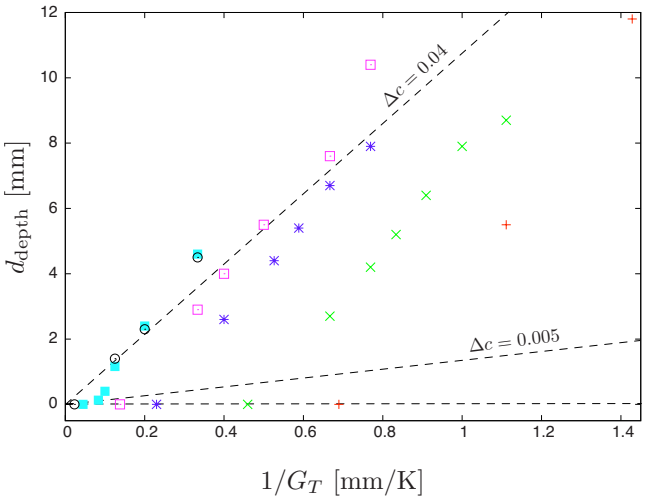

FIG. 7. (Color online) Cell depth $d_{\rm depth}$ as a function of the inverse temperature gradient $1/G_T$ for different diffusion constants $D_{\rm Si}$. From left to right: 1.0×10^{-9} m^2/s (open circles), 1.94×10^{-9} m^2/s (filled squares), 6×10^{-9} m^2/s (open squares), 1×10^{-8} m^2/s (stars), 2×10^{-8} m^2/s (crosses), and 3×10^{-8} m^2/s (plus signs).

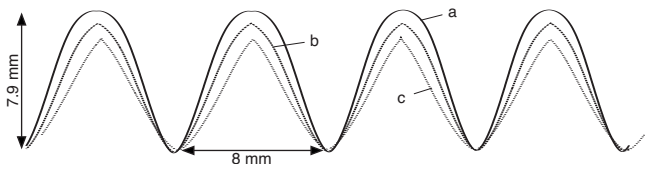

FIG. 8. Cell shapes for (a) $D_{\rm Si}=1\times10^{-8}$ m^2/s, $v_{\rm pull}=6$ mm/h, (b) $D_{\rm Si}=2\times10^{-8}$ m^2/s, $v_{\rm pull}=12$ mm/h, and (c) $D_{\rm Si}=3\times10^{-8}$ m^2/s, $v_{\rm pull}=18$ mm/h. All other parameters were the same in both runs ($G_T=1.3$ K/mm). Cell tips are at the bottom. The straight line is the interface in case (a), the middle dashed line is the one in case (b) and the one at bottom represents the interface in case (c).

temperature difference ΔT is related to the difference in Si concentration Δc via the phase diagram. Using the linearized equation (36) we can express the concentration difference as

$$\Delta c = G_T d_{\rm depth}/270 \ {\rm K}^{-1}. \quad (40)$$

Two lines of constant Δc according to this equation are shown in Fig. 7. The line of $\Delta c=0.005$ is given because in the crystals grown the difference in concentration is less than this value [39]. Consequently, this would require a large temperature gradient at the interface which can be estimated not to be the case in the experiments. However, in the experiments a strong melt flow is present and this will have a significant impact on the pattern formation. First results are discussed in [39,40].

The other line in Fig. 7 ($\Delta c=0.04$) represents a critical line, because the average concentration in the crystal is $c=0.02$ and in a system with equally distributed Si concentration the maximum difference in c is 0.04. Beyond this line the interface at the inner part of the cell becomes unstable. This is shown for $D_{\rm Si}=1.94\times10^{-9}$ m^2/s in Fig. 11, where also the concentration profile along three lines is shown. For $G_T=5$ K/mm (bottom) the cell depth is below the critical line and the concentration profile in the crystal is of a nearly sinusoidal profile (Fig. 11 right bottom). For $G_T=3$ K/mm (top) the profile becomes quite different and the cell tip is sharper in the first case, with a larger radius at the bottom.

The strength of anisotropy in the surface energy has only a minor influence on the steady-state shape of the interface. We used an anisotropy of $\varepsilon=0.03$ and $\varepsilon=0.25$ and observed the same shape of the interface though there are some differences during the onset of the instabilities. A difference is only observed in the cases with side arms, which will be discussed later.

We can rewrite Eq. (38) in terms of dimensionless values:

$$\tilde{d}_{\rm depth} = \left(\frac{1}{\tilde{G}_T} - \frac{1}{\rm Pe}c_T\right). \quad (41)$$

Here, we rescaled all lengths by d_0 and the temperature by $\Delta_d T$, i.e., $\tilde{G}_T = G_T d_0/\Delta T_0$. c_T is the relation between $\Delta_d T$ and ΔT_0. The dimensionless depth $\tilde{d}_{\rm depth}$ is in the order of 10^7. Since all results for deriving Eq. (38) have been observed with a growth kinetics faster than the growth velocity of the interface ($v_{\rm pull}=6$ mm/h) also Eq. (41) is valid only for such cases.

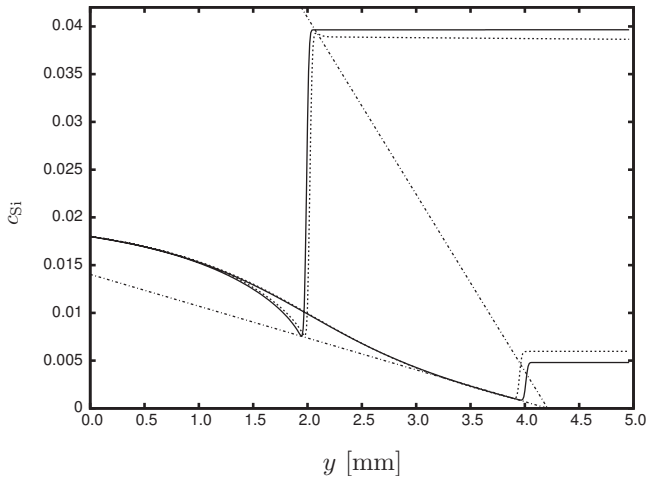

FIG. 9. Comparison of concentration profiles at top and bottom of cells for two different functions of D_{Si} in the diffuse interface. Dotted line: Eq. (29), solid line: Eq. (30). The straight lines represents the liquidus and solidus concentration according to the temperature field and the phase diagram.

In order to minimize the computational costs we used a kinetic coefficient as small as possible, which guarantees still a growth kinetics faster than the macroscopic growth velocity. Due to Eq. (33) there is a linear relation between the inverse of the kinetic coefficient and the maximal possible time step. We chose $\mu=5\times10^{-6}$ m/(s K) and checked numerically for distinguished cases that a larger kinetic coefficient does not change the result. The influence of finite growth kinetics can be seen when increasing the growth velocity and keeping the kinetic coefficient constant. We chose three different pulling velocities $v_{pull}=6$, 12, and 18 mm/h keeping the Peclet number constant by choosing corresponding diffusion coefficients $D_{Si}=1\times10^{-8}$, 2×10^{-8}, and 3×10^{-8} m^2/s, respectively. The temperature gradient was $G_T=1300$ K/m. The larger the growth velocity is the sharper the tip is at the top of the cell (Fig. 8).

In contrary to investigations on the μm scale, the width of the diffuse interface in our case is rather thick compared to the diffusion length. Therefore, we checked the influence of the different interpolation schemes for the diffusion constant D_{Si}. In Fig. 9 we show the analysis for $D_{Si}=1.94\times10^{-9}$ m^2/s and $G_T=5$ K/mm: the concentration profiles along the two lines normal to the surface (as indicated in Fig. 11) are plotted. Small differences can be observed. In the linear interpolation [Eq. (29)] a slight overshooting in concentration at the diffuse interface is present. This is completely removed when using Eq. (30). The depth of the cells is slightly larger in second case ($d_{depth}=2.02$ mm) than in the first one ($d_{depth}=1.97$ mm). Therefore, also the concentration variation is larger: $\Delta c=0.0349$ when using Eq. (30) and $\Delta c=0.0327$ when using Eq. (29). The theoretical values computed by using Eq. (36) are larger in both cases ($\Delta c_{theor}=0.0374$ and $\Delta c_{theor}=0.0365$). The difference between theoretical and numerical value is due to the finite width of the interface. In the current example the temperature drop within the diffuse interface is 0.5 K, which corresponds to a concentration drop of 0.002 in the melt. The results in Fig. 7 were obtained using Eq. (30).

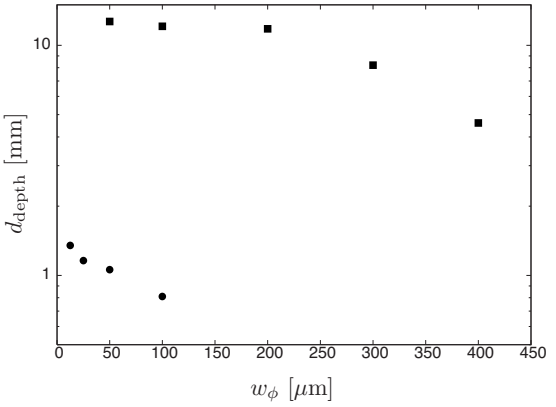

FIG. 10. (Color online) Depth of the cells for two different cases: $D_{Si}=3\times10^{-8}$ m^2/s, $G_T=0.7$ K/mm (filled circles) and $D_{Si}=1.94\times10^{-9}$ m^2/s, $G_T=8.0$ K/mm (filled boxes).

2. Secondary arm spacing

For the case beyond the critical line ($\Delta c=0.04$ in Fig. 7) the instabilities at the inner interface are much pronounced if we use Eq. (30) and a secondary arm spacing is observed (see Fig. 12). Secondary arm spacing is well known from other systems. From theoretical considerations and experiments Billia *et al.* derived an expression for the critical growth velocity, where the cellular growth changed to a dendritic one [41]. Rewriting this equation in terms of a critical inverse temperature gradient $(1/G_T)_{c->d}$ in relation the critical inverse temperature gradient $(1/G_T)_{cr}$ for the planar-to-cellular growth transition one gets:

$$(1/G_T)_{c->d} = \sqrt[4]{\frac{\alpha}{k\mathrm{Pe}}}(1/G_T)_{cr}, \tag{42}$$

where α is a constant characteristic for a particular material system. Several theoretical and experimental work has been done on analyzing the secondary arm spacing (see, e.g., [42]). Estimating the factor of $(1/G_T)_{cr}$ in Eq. (42) for our cases with $\alpha=1$ we get a factor near to 100. This means we should not observe secondary arm spacing for all the runs we have performed. Indeed, after the originally planar interface becomes unstable and the first small structures formed no secondary arm spacing occurred. Looking more carefully to the growth behavior in the early stage of runs near the critical line $\Delta c=0.04$ one can observe a fingerlike growth. There is a high concentration of Si in the solidified fingers and a small concentration at the bottom of the grooves. Some planes at the sides of the solidified fingers are almost parallel to the temperature gradient. The temperature gradient normal this plan is almost zero and when this plane starts to grow the interface becomes immediately unstable. If we consider the line of $\Delta c=0.04$ as the critical line for the transition from cellular to dendritic growth, we can derive an expression for the critical inverse temperature gradient $(1/G_T)_{c->d}$ of this transition. Using Eqs. (40) and (38) we obtain

$$(1/G_T)_{c->d} = (1/G_T)_{cr}\frac{\Delta_d T}{\Delta_d T - 270\ \mathrm{K}\Delta c}. \tag{43}$$

In our case ($\Delta c=0.04$) we get $(1/G_T)_{c->d}=2.9(1/G_T)_{cr}$. Equation (43) does not depend on the Pe number of the

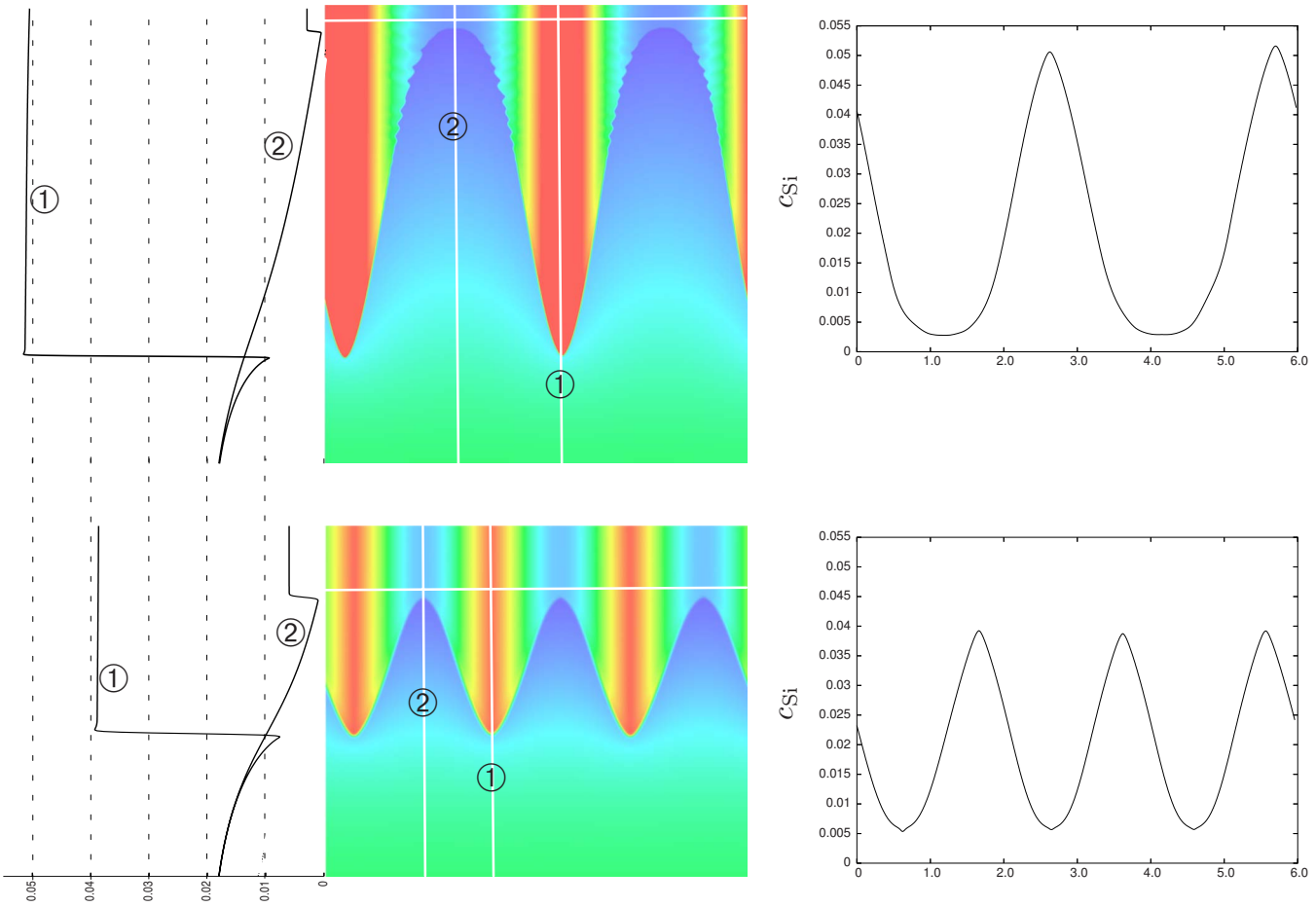

FIG. 11. Shape of cells and concentration distributions for $D_{Si}=1.94\times10^{-9}$ m^2/s and two temperature gradients in the vicinity of Δc_{crit}: $G_T=3$ K/mm (top) and $G_T=5$ K/mm (bottom). On the very left the concentration profile along two lines is presented. On the right-hand side the profiles of Si along the horizontal lines is shown. The colors/grey shadings in the middle pictures correspond to c_{Si}.

system. Please notice that Eq. (43) was derived from the numerical results for an averaged concentration in the solid of $\bar{c}_s=0.02$ and a fixed relation of the kinetic coefficient to the growth velocity.

Because in the runs beyond $\Delta c=0.04$ small structures remain during the evolution of the cell structures surface tension has an influence on the long time development. If the anisotropy is increased from $\varepsilon=0.03$ to $\varepsilon=0.25$ in the run for $D_{Si}=1.94\times10^{-9}$ m^2/s and $G_T=3$ K/mm (see Fig. 12) a third finger remains and the amplitudes of the secondary arm spacings are smaller (computations have been performed up to 1 h 23 min physical time).

3. Wave length

From the viewpoint of applications the cell depth is the most interesting quantity of the computation, because it determines directly the concentration variation in the grown crystal. However, besides the vertical length scale there is the lateral one, namely the wave length of the structures. Because of the periodic boundary condition the width of the domain should be as large as possible but the computational costs limit the extend. In our calculations we had 4–9 cells in a computational domain, which means one has to expect errors of 10–20 % for the wave length.

We checked the dependence of the wave length λ on the cell depth d_{depth} and found that λ increases linearly with the square root of d_{depth} (see Fig. 13), which can be written as

$$\lambda = \lambda_0 + \sqrt{a_\lambda}\sqrt{d_{depth}}, \tag{44}$$

with $\lambda_0=(-3\mp1)$ mm and $a_\lambda=(21\mp10)$ mm. Runs with a $\Delta c>0.04$ (marked by ellipses in Fig. 13) seem to obey the

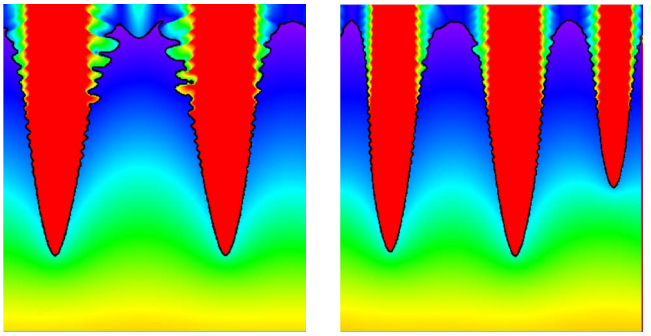

FIG. 12. (Color online) Cell shapes for $D_{Si}=1.9\times10^{-9}$ m^2/s and $G_T=3$ K/mm. Different morphologies are observed if using an anisotropy $\varepsilon=0.03$ (left) or $\varepsilon=0.25$ (right).

same rule [Eq. (44)] but with a different λ_0. For cellular growth the following equation has been derived by geometric considerations (see, e.g., p. 83 in [38]):

$$\lambda = 2\sqrt{d_{\text{depth}} a_{\text{shape}} R_{\text{tip}}}, \tag{45}$$

where a_{shape} is a geometric factor taking into account the shape of the tip ($a_{\text{shape}}=1$ for elliptic and $a_{\text{shape}}=2$ for parabolic shape). Thus, in all cases the wavelength is proportional to the square root of the cell depth. However, the different shapes at the bottom of the cells lead to a different shift λ_0. For $d_{\text{depth}} \to 0$ the wavelength should also vanish, i.e., $\lambda_0=0$ as it is in Eq. (45).

4. Influence of interface thickness

We tested the dependence of the structure on the thickness w_ϕ of the diffuse interface by increasing the number of mesh points in the computational domain. The number of grid points in the diffuse interface was fixed to 10 and the growth dynamics was the same for all computations, i.e., D^*_ϕ [see Eq. (32)] was kept constant ($D^*_\phi=0.24$). In Fig. 10 we present the results for high diffusivity and low-temperature gradient ($D_{\text{Si}}=3\times10^{-8}$ m^2/s, $G_T=0.7$ K/mm) and for low diffusivity and high-temperature gradient ($D_{\text{Si}}=1.94\times10^{-9}$ m^2/s, $G_T=8.0$ K/mm). Constant D^*_ϕ means that the time step is also changing when changing the resolution. The influence of the time step with constant resolution can be seen from Table V. Here also three calculations with different domain width are presented. For $n_x=1000$ and $n_x=1300$ there are only two cells in the domain, for $n_x=3000$ there are six.

VI. CONCLUSIONS

We developed a modified phase field method, which enables us to calculate cellular structures in the range of μm to mm. The method has been tested for several cases, where analytic solutions are known. The main focus of the paper is on a detailed study of pattern formation in a $Ge_{1-x}Si_x$ system. One of the critical material parameters in the evolution of the cellular structures is the diffusion coefficient of Si in the Ge-rich melt. We used MD calculations in order to obtain diffusion coefficients for different compositions of the melt.

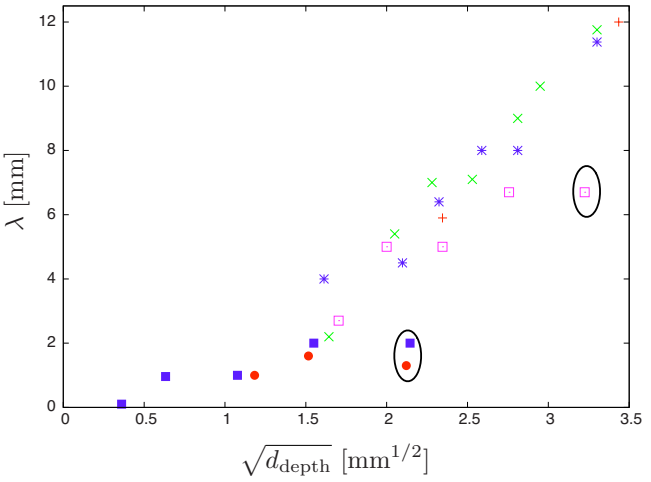

FIG. 13. (Color online) Wave length versus square root of cell depth for pulling velocity $v_{\text{pull}}=6$ mm/h. From left to right: 1.0×10^{-9} m^2/s (filled circles), 1.94×10^{-9} m^2/s (filled squares), 6×10^{-9} m^2/s (open squares), 1×10^{-8} m^2/s (stars), 2×10^{-8} m^2/s (crosses), and 3×10^{-8} m^2/s (plus signs). Points marked by an ellipse are for values beyond the line of $\Delta c=0.04$ (compare with Fig. 7).

Our calculations are in agreement with those of other computations but they are smaller than those obtained by experiments. In order to test the sensibility of the growth system on the diffusion coefficient we have performed runs with different diffusion constants and also for different temperature gradients. For all diffusion coefficients we found the same linear relationship between the inverse of the temperature gradient and the cell depth. The cell depth becomes zero at the critical value of the inverse temperature gradient, which was obtained from perturbation theory. Except for very small wave length of the cellular structure, the wave length is proportional to the square root of the cell depth regardless of the diffusion coefficient and temperature gradient used.

ACKNOWLEDGMENT

We would like to thank an anonymous referee for most valuable hints.

TABLE V. Results of different runs for $D_{\text{Si}}=3\times10^{-8}$ m^2/s and $G_T=700$ K/m.

$n_x\times n_y$	Δx (μm)	Δt (ms)	D^*_φ	d_{depth} (mm)	λ (mm)
3000×1000	20.0	320	0.24	11.8	12.0
3000×750	20.0	300	0.225	9.9	10.0
3000×750	20.0	150	0.113	10.0	10.0
2250×560	30.0	675	0.225	9.2	13.5
2250×560	30.0	338	0.113	9.6	13.5
1500×400	40.0	1280	0.24	5.4	8.6
1500×400	40.0	320	0.06	8.2	12.0

[1] N. V. Abrosimov, Exp. Astron. **20**, 185 (2005).
[2] H. Halloin *et al.*, Nucl. Instrum. Methods Phys. Res. A **504**, 120 (2003).
[3] O. Penrose and P. C. Fife, Physica D **43**, 44 (1990).
[4] G. Caginalp, in *Applications of Field Theory to Statistical Mechanics*, Lecture Notes in Physics Vol. 216, edited by L. Garrido (Springer-Verlag, Berlin, 1985), pp. 216–226.
[5] A. Karma, Phys. Rev. Lett. **87**, 115701 (2001).
[6] S. G. Kim, W. T. Kim, and T. Suzuki, Phys. Rev. E **60**, 7186 (1999).
[7] A. A. Wheeler, W. J. Boettinger, and G. B. McFadden, Phys. Rev. A **45**, 7424 (1992).
[8] R. Folch and M. Plapp, Phys. Rev. E **68**, 010602(R) (2003).
[9] A. A. Wheeler, G. B. McFadden, and W. J. Boettinger, Proc. R. Soc. London, Ser. A **452**, 495 (1996).
[10] B. Echebarria, R. Folch, A. Karma, and M. Plapp, Phys. Rev. E **70**, 061604 (2004).
[11] S.-L. Wang, R. F. Sekerka, A. A. Wheeler, S. R. Coriell, R. J. Braun, and G. B. McFadden, Physica D **69**, 189 (1993).
[12] A. Karma and W.-J. Rappel, Phys. Rev. E **57**, 4323 (1998).
[13] Y.-T. Kim, N. Provatas, N. Goldenfeld, and J. Dantzig, Phys. Rev. E **59**, R2546 (1999).
[14] G. B. McFadden, A. A. Wheeler, R. J. Braun, S. R. Coriell, and R. F. Sekerka, Phys. Rev. E **48**, 2016 (1993).
[15] R. F. Sekerka, in *Crystal Growth from Fundamentals to Technology*, edited by G. Müller, J.-J. Métois, and P. Rudolph (Elsevier, New York, 2004), pp. 55–93.
[16] W. Miller, I. Rasin, and S. Succi, Trends Stat. Phys. **4**, 123 (2004).
[17] A. Karma and W.-J. Rappel, Phys. Rev. E **53**, R3017 (1996).
[18] I. Rasin, S. Succi, and W. Miller, J. Comput. Phys. **206**, 453 (2005).
[19] I. Rasin, W. Miller, and S. Succi, Phys. Rev. E **72**, 066705 (2005).
[20] W. J. Boettinger and J. A. Warren, J. Cryst. Growth **200**, 583 (1999).
[21] C. W. Lan and Y. C. Chang, J. Cryst. Growth **250**, 525 (2003).
[22] H. Okamoto, *Phase Diagrams for Binary Alloys* (American Society for Metals, Metals Park, OH, 2000).
[23] H. Stöhr and W. Klemm, Z. Anorg. Allg. Chem. **241**, 305 (1939).
[24] V. N. Romanenko and Y. M. Smirnov, Neoorganskij Materialy **10**, 1733 (1970) in Russian.
[25] J. P. Dismukes and W. M. Yim, J. Cryst. Growth **22**, 287 (1974).
[26] P. G. Sanders and M. J. Aziz, J. Appl. Phys. **86**, 4258 (1999).
[27] E. Ko, M. Jain, and J. R. Chelikowsky, J. Chem. Phys. **117**, 3476 (2002).
[28] M. O. Thompson, P. S. Peercy, J. Y. Tsao, and M. J. Aziz, Appl. Phys. Lett. **49**, 558 (1986).
[29] R. V. Kulkarni, W. G. Aulbur, and D. Stroud, Phys. Rev. B **55**, 6896 (1997).
[30] S. Munejiri, F. Shimojo, K. Hoshino, and T. Itami, J. Non-Cryst. Solids **312-314**, 182 (2002).
[31] V. Godlevsky, J. R. Chelikowsky, and N. Troullier, Phys. Rev. B **52**, 13281 (1995).
[32] N. Takeuchi and I. L. Garzón, Phys. Rev. B **50**, 8342 (1994).
[33] F. H. Stillinger and T. A. Weber, Phys. Rev. B **31**, 5262 (1985).
[34] Q. Yu and P. Clancy, J. Cryst. Growth **149**, 45 (1995).
[35] Q. Yu and P. Clancy, Modell. Simul. Mater. Sci. Eng. **2**, 829 (1994).
[36] Q. Yu, M. O. Thompson, and P. Clancy, Phys. Rev. B **53**, 8386 (1996).
[37] W. Yu, Z. Q. Wang, and D. Stroud, Phys. Rev. B **54**, 13946 (1996).
[38] W. Kurz and D. J. Fisher, *Fundamentals of Solidification* (Trans Tech, Uetikon-Zürich, 1998).
[39] W. Miller, N. Abrosimov, I. Rasin, and D. Borissova, J. Cryst. Growth **310**, 1405 (2008).
[40] W. Miller and I. Rasin, J. Cryst. Growth **303**, 95 (2007).
[41] B. Billia, H. Jamgotchian, and R. Trivedi, J. Cryst. Growth **106**, 410 (1990).
[42] D. M. Rosa, J. E. Spinelli, I. L. Ferreira, and A. Garcia, Metall. Mater. Trans. A **39**, 2161 (2008).